

# Structure, electrical characteristics, and high-temperature stability of aerosol jet printed silver nanoparticle films

Md Taibur Rahman,<sup>1</sup> John McCloy,<sup>1</sup> C. V. Ramana,<sup>2,a)</sup> and Rahul Panat<sup>1,a)</sup>

<sup>1</sup>*School of Mechanical and Materials Engineering, Washington State University, Pullman, Washington 99163, USA*

<sup>2</sup>*Department of Mechanical Engineering, University of Texas at El Paso, El Paso, Texas 79968, USA*

(Received 8 May 2016; accepted 31 July 2016; published online 17 August 2016)

Printed electronics has emerged as a versatile eco-friendly fabrication technique to create sintered nanoparticle (NP) films on arbitrary surfaces with an excellent control over the film microstructure. While applicability of such films for high-temperature applications is not explored previously, herein we report the high-temperature electrical stability of silver (Ag) metal NP films fabricated using an Aerosol Jet based printing technique and demonstrate that this behavior is dictated by changes in the film microstructure. *In-situ* high temperature (24–500 °C) impedance spectroscopy measurements show that the real part of the impedance increases with increasing temperature up to 150 °C, at which point a decreasing trend prevails until 300 °C, followed again by an increase in impedance. The electrical behavior is correlated with the *in-situ* grain growth of the Ag NP films, as observed afterwards by scanning electron microscopy and X-ray diffraction (XRD), and could be tailored by controlling the initial microstructure through sintering conditions. Using combined diffraction and spectroscopic analytical methods, it is demonstrated the Aerosol Jet printed Ag NP films exhibit enhanced thermal stability and oxidation resistance. In addition to establishing the conditions for stability of Ag NP films, the results provide a fundamental understanding of the effect of grain growth and reduction in grain boundary area on the electrical stability of sintered NP films. *Published by AIP Publishing*. [<http://dx.doi.org/10.1063/1.4960779>]

## I. INTRODUCTION

*In-situ* monitoring of combustion parameters at high temperature in Fossil Energy (FE) based power generation systems can lead to several benefits in energy efficiency and safety.<sup>1</sup> For example, the fuel consumption of the systems can be improved through a continuous feedback loop of combustion parameters to the fuel injector.<sup>2,3</sup> While such monitoring and feedback can potentially lead to transformative improvements, *in-situ* measurements of the system parameters are not straightforward due to the extreme operating temperatures for the electronics and the related materials and manufacturing challenges.<sup>4</sup> Further, the components of the high temperature systems have complex 3-D shapes, making the fabrication of the electronics highly challenging.<sup>2</sup> Conventional photolithography/MEMS based sensor electronics are limited in their ability to conform to the 3-D shapes<sup>5</sup> as well as the choices of materials<sup>6</sup> that can survive a high temperature in the FE environments.

In contrast to the conventional methods, printed electronics (i.e., microscale additive manufacturing) methods such as the Aerosol Jet (AJ)<sup>7</sup> printing are being developed to fabricate electronic materials and a wide variety of architectures. These methods will allow fabricating such architectures at the micro- and nanometer length scales on not only the flat surfaces and routine electronics but also the highly complicated, arbitrary curved surfaces. Such methods provide fast, inexpensive, and environmentally friendly patterning of nanoparticle (NP)

based films.<sup>8</sup> These films, when sintered, can exhibit an electrical conductivity of up to 50% of the bulk value<sup>9</sup> and have a very high surface to volume ratio that may help to reduce the build-up of stresses. The AJ method utilizes a mist of NP inks directed by a carrier gas, and can print inks with viscosities up to 1000 cP and feature sizes down to 10 μm. Furthermore, it has already been used to manufacture biosensors,<sup>10</sup> capacitive sensors,<sup>11</sup> transistors,<sup>12</sup> solar cells,<sup>13,14</sup> electronic interconnects,<sup>15</sup> and 3-D antenna structures.<sup>9</sup> The particle size in the inks used in the AJ method is typically <500 nm and has a printing standoff height of 5 mm,<sup>9</sup> enabling the production of electronic circuits on complex 3-D surfaces.

The 3-D printed film materials for high temperature electronic applications need to be readily available in NP form, have predictable and repeatable electrical properties, and have a high conductivity. Silver (Ag) NP films are of considerable interest as potential candidates for such applications as the silver bulk electrical resistivity is lower than most other commonly used conductive materials. The silver also has a higher electro-migration resistance in electronic devices when compared to other conductive NP based materials such as Al.<sup>16</sup> Note that the oxidation behavior of Ag NP films at high temperature can be evaluated to ensure that its electrical properties are consistent even if the oxide layer forms. Silver thin films fabricated on various substrates using physical vapor deposition methods have been studied in the past for high temperature applications.<sup>17,18</sup> An agglomeration behavior of Ag films was reported at high temperature, where diffusional creep was believed to cause the film to form holes and

<sup>a)</sup>Authors to whom correspondence should be addressed. Electronic addresses: rahul.panat@wsu.edu and rvchintalapalle@utep.edu

hillocks due to the film residual stresses.<sup>18</sup> Kim *et al.*<sup>17</sup> performed *in-situ* resistance measurement on evaporated silver thin films of less than 100 nm thickness at temperatures up to 600 °C. They found that thicker films showed a stable resistance up to 600 °C with films <70 nm in thickness showing a resistance increase with temperature. The room temperature resistance along with the microstructure of aerosol jet printed and inkjet printed silver NP lines sintered under different conditions up to 300 °C was characterized by Seifert *et al.*<sup>19</sup> Their work showed that the room temperature resistance of the lines decreases with higher sintering temperature along with an increase in the grain size as observed under a scanning electron microscopy (SEM). None of the above works investigated the frequency response of such films *in situ* at high temperature, though these characteristics would be important in electronic applications, including sensors and antennas. The sintering process of the silver thiolate (surfactant) encapsulated NPs was studied by Volkman *et al.*<sup>20</sup> at a temperature of 200 °C for 15 min. They observed that the surfactants were present during the entire sintering process and influenced the film grain size and crystallite orientation. Greer and Street developed a sintering model, where the resistivity change of the NP films was correlated with the particle densification and film thickness changes.<sup>21</sup> Note that the typical thickness of electronic interconnects (e.g., PCBs) or sensor films is >1 μm, and the impedance behavior of such films fabricated by NP based methods is yet unexplored. Further, the influence of the initial particle size on the evolution of the grain growth in such films is expected to influence their properties and needs to be studied.

The impetus for the present work is two-fold. First, we aimed to synthesize high quality Ag NP films using Aerosol Jet printing. Second, we desire a fundamental understanding of such printed Ag NP film microstructure, electrical characteristics, and thermal oxidation behavior, in order to demonstrate their applicability for high temperature sensor electrode applications. In this paper, we investigate the electrical properties of Aerosol Jet printed Ag NP films at a temperature range of 24–500 °C and at a frequency range of 0.02–300 kHz. Microstructural evolution of the Ag NP films has been studied by employing scanning electron microscopy (SEM), X-ray diffraction (XRD), and X-ray photoelectron spectroscopy (XPS) and correlated with the electrical behavior. Using the results as presented and discussed, the high temperature thermal stability and oxidation resistance behavior of AJ printed Ag NP films is demonstrated. In addition, it is shown that the microstructural changes influence the electrical properties of the Ag NP films and could be controlled by the initial sintering conditions, which can ultimately result in favorable, tunable properties of printed Ag NP films.

## II. EXPERIMENTAL DETAILS

An Aerosol Jet based micro-additive printer (AJ-300, Optomec Inc., Albuquerque, NM) was used to fabricate the Ag NP films. The AJ method allows the deposition of NPs dispersed in a solvent (i.e., NP ink) onto a substrate by creating a mist of particles guided by a carrier gas. The AJ printing system includes two atomizers (ultrasonic and pneumatic), a

programmable XY motion stage, and a deposition head. A solvent-based Ag NP ink (Perfect-TPS 50 G2, Clariant Group, Frankfurt, Germany) was placed in the atomizer which continuously created the mist with droplet sizes of 1–5 μm (each droplet containing multiple NPs) which were then carried to the deposition head with a carrier N<sub>2</sub> gas.<sup>22</sup> The mist or dense vapor was then focused and driven towards the nozzle with the help of a secondary gas (also N<sub>2</sub>) to form a micro-jet. The silver NP size in the ink was 30–50 nm, the particle loading in the ink was 40 ± 2 wt. %, and the viscosity was about 1.5 cP. To prevent particle agglomeration, ink material was placed in a tube which was rotated continuously around its axis for at least 12 h using a tube roller (Scilogex MX-T6-S, Rocky Hill, CT) prior to printing. A transparent glass slide (Thermo-Fisher Scientific, Waltham, MA) was used as the substrate. Prior to printing, the substrates were cleaned with deionized water followed by isopropyl alcohol. The substrate surface was then cleaned using an atmospheric O<sub>2</sub> plasma (Atomflo™ 400, SurfX® Technologies LLC, Redondo Beach, CA) at 100 W power for 5 min to increase the surface hydrophilicity and adhesion with the printed film.

The Ag NP ink was dispensed on the glass substrate using the ultrasonic atomizer. Before printing, the geometry of the conductive part was drawn in AutoCAD (AutoCAD 2015, Autodesk, Inc., San Rafael, CA) and converted to a “.prg” file compatible with the printer software. The nozzle exit diameter used to print Ag films was 200 μm. An atomizing flow rate of 25 sccm and a sheath gas flow rate of 50 sccm were used for printing. The printed pattern was thermally sintered in a programmable oven (Neytech Vulcan furnace, Model 3–550, Degussa-Ney Dental, Inc., Bloomfield, CT) at 200 °C for 30 min, or 30 min followed by 6 h, depending upon the experiment. The film profile was characterized using a contact profilometer (DekTak-XT, Bruker Instruments, San Jose, CA). The grain boundary (GB) grooving was characterized using an Atomic Force Microscope (AFM) (Dimension Icon, Bruker Corporation, Billerica, MA).

Phase identification, crystal structure, and oxidation behavior of the Ag NP film was analyzed with an X-ray diffractometer (PANalytical, EA Almelo, Lelyweg, Netherlands). Measurements were made at room temperature using Cu K $\alpha$  radiation ( $\lambda = 1.5406 \text{ \AA}$ ). The film oxidation behavior was further analyzed by X-ray Photoelectron Spectroscopy (XPS) (Pelkin Elmer Corporation, Waltham, MA). XPS spectra were taken at room temperature using Mg K $\alpha$  radiation. Survey as well as core-level spectra of Ag 3d were recorded as a function temperature in order to probe the chemical changes, especially oxidation, under thermal exposure. To measure the electrical properties, Pyro-duct 597-A conductive epoxy (Aremco, Valley Cottage, NY) was used to connect the wires with the samples. Conductive epoxy was ambient cured overnight followed by heat cure at 93 °C for 2 h. A signal of 1 V and frequency in the range of 0.02–300 kHz was applied using a precision LCR meter (Agilent E4980A) with a 4-wire measurement. Before each measurement, a standard calibration method was performed to remove any parasitic effects. The Vulcan 3–550 high temperature furnace was used to heat the samples during the *in-situ* impedance measurements. Dwelling

time for each temperature was 10 min, after which the impedance was measured.

### III. RESULTS AND DISCUSSION

An optical image of a representative printed Ag NP film (7 mm long and  $540\ \mu\text{m}$  wide) with probing pads, sintered at  $200\ ^\circ\text{C}$  for 30 min is shown in Fig. 1(a). A 3-D profilometer scan of a segment of the Ag NP film is shown in Fig. 1(b). Figure 1(c) shows a line scan of one of the slices in Fig. 1(b). The peak at the center of the scan is consistent with the tool path of the machine used to fill the film area. Figure 1(d) shows the width variation of the film to be within  $\pm 2.5\%$ . The nominal height of the AJ printed Ag NP films was about  $17\ \mu\text{m}$ .

#### A. Impedance spectroscopy

The impedance data of the as-sintered Ag NP film (sintered at  $200\ ^\circ\text{C}$  for 30 min) at various frequencies and temperatures are shown in Fig. 2. The real part of impedance,  $Z'$ , at temperatures ranging from  $24\ ^\circ\text{C}$  to  $500\ ^\circ\text{C}$  at intervals of  $50\ ^\circ\text{C}$  are presented in Fig. 2(a). At ambient conditions,  $Z'$  does not increase in frequency up to about 30 kHz and moderately increases by about 40% up to 300 kHz. A monotonous increase in  $Z'$  was observed with an increase in the temperature up to about  $150\ ^\circ\text{C}$ . This is consistent with the positive temperature coefficient of resistance (TCR) of silver. The TCR value determined in this work based upon measurements in the  $24\text{--}150\ ^\circ\text{C}$  temperature range is

$0.000302\ /^\circ\text{C}$  (at 20 Hz) while that of bulk Ag is  $0.0038\ /^\circ\text{C}$  at room temperature.<sup>23</sup> The TCR value for nanostructured Ag is  $\sim 0.0004\ /^\circ\text{C}$  at  $27\ ^\circ\text{C}$ .<sup>23</sup> Thus, the TCR value determined in the present work for AJ printed Ag NP films is comparable to that reported for nanostructured Ag rather than that reported for bulk Ag. This observation is independent of the frequency. Upon further heating, the  $Z'$  dropped by an order of magnitude until about  $300\ ^\circ\text{C}$  at all frequencies. Beyond this temperature, the  $Z'$  increases again with increasing temperature (positive TCR), up to  $500\ ^\circ\text{C}$ . The TCR in this temperature range is  $\sim 0.00156\ /^\circ\text{C}$  (at 20 Hz), or an order of magnitude higher than that observed at low temperatures. We will return to this apparent negative TCR between  $150$  to  $300\ ^\circ\text{C}$  ( $-0.0059\ /^\circ\text{C}$ , at 20 Hz) in the latter part of this section as it is to be related to microstructural changes to the film. Figure 2(b) shows the  $Z'$  as function of temperature for different frequencies showing the drop in  $Z'$  between  $150\ ^\circ\text{C}$  and  $300\ ^\circ\text{C}$  discussed above. Figure 2(c) shows the imaginary part of impedance,  $Z''$ , as a function of temperature. The  $Z''$  remained unchanged as a function of temperature. This behavior can be understood from the fact that the  $Z''$  primarily represents inductive losses in the circuit and is expected to be dependent upon the frequency alone. The TCR as a function of temperature is shown in Fig. 2(d). The behavior described in Fig. 2 was found to be repeatable over several Ag NP films tested.

It is well-known that the positive TCR for metals results from an increase in atomic vibrations that increase the electron scattering and hence resistance at higher temperatures.

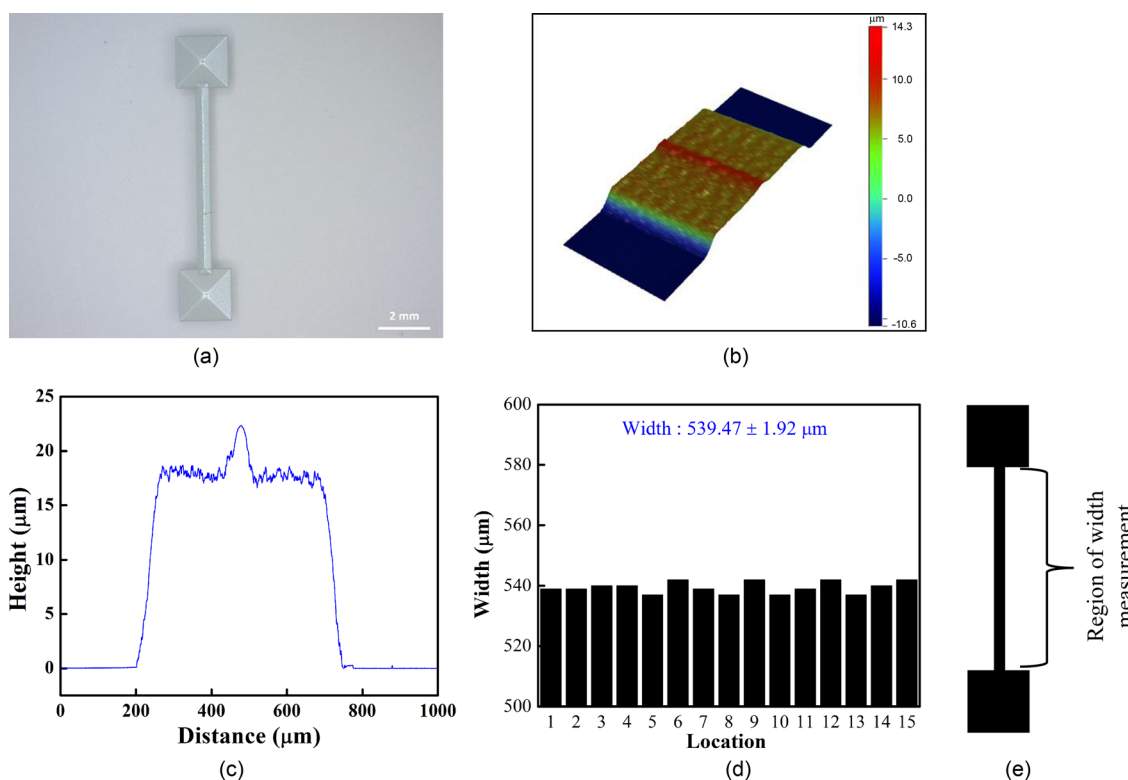


FIG. 1. (a) Optical image of a printed Ag film, (b) 3-D profilometer scan of a segment of a printed Ag film, (c) a line scan across a segment of the printed Ag film showing a nominal height of  $\sim 17\ \mu\text{m}$ , and (d) width variation of printed Ag film measured at 5 locations/sample over 3 samples. A variation of  $\pm 1.92\ \mu\text{m}$  indicates high printing accuracy of the Aerosol Jet system. (e) Schematic showing the segment of the printed Ag film where the width measurements were performed.

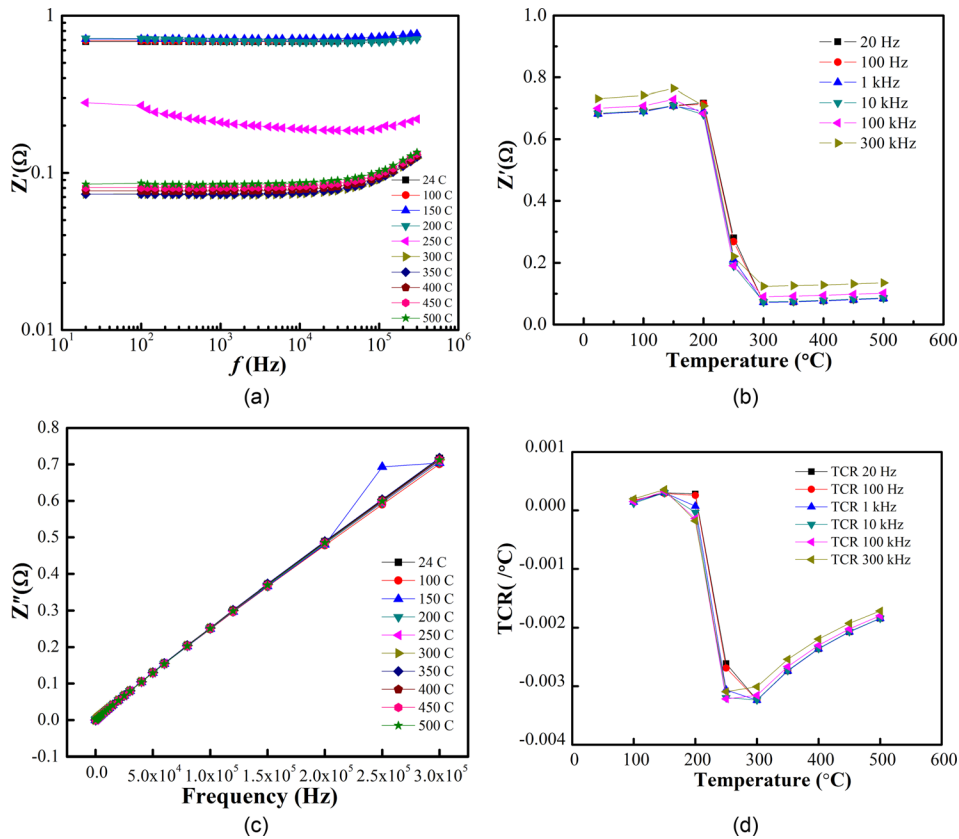


FIG. 2. Electrical behavior of Ag NP film at different temperatures (24 to 500  $^{\circ}\text{C}$ ) and frequencies (0.02–300 kHz). A film sintering condition of 200  $^{\circ}\text{C}$  for 30 min was applied prior to the electrical measurements. (a) The real part of impedance ( $Z'$ ) measured as a function of frequency at intervals of about 50  $^{\circ}\text{C}$ . (b) The real part of impedance ( $Z'$ ) as a function of temperature. (c) Imaginary part of impedance ( $Z''$ ) as a function of frequency. (d) TCR as a function of temperature.

The frequency dependence of electrical conductivity is defined by the following equation:<sup>24</sup>

$$\sigma(\omega) = \sigma(0) \left( \frac{1 + i\omega\tau}{1 + (\omega\tau)^2} \right), \quad (1)$$

where  $\sigma(0) = \frac{ne^2\tau}{m}$ ,  $m$  is the effective mass of the electron,  $n$  is the number of electrons,  $\tau$  is the collision time,  $\omega$  is the frequency, and  $e$  is the charge on the electron. The conductivity thus increases with frequency (at a given temperature) resulting in an increase in  $Z'$  as seen in Figs. 2(a) and 2(b). The unstable behavior of  $Z'$  as shown in Figs. 2(a) and 2(b) will affect its usability in high temperature electronic applications. Sintering conditions of 150–200  $^{\circ}\text{C}$  for  $\leq 30$  min have been typically used while creating highly conductive films for various applications in printed electronics.<sup>20,21,25,26</sup> In order to further understand the effect of sintering conditions on the electrical behavior of the films, we prepared Ag NP samples with sintering conditions of 200  $^{\circ}\text{C}$  for 30 min, followed by 200  $^{\circ}\text{C}$  for 6 h (i.e., post-processed the sample compared to the ones used to collect data shown in Fig. 2). Fig. 3(a) shows the impedance behavior of the post-processed sample. Unlike the behavior seen in Figs. 2(a) and 2(b), the  $Z'$  increased from room temperature to 500  $^{\circ}\text{C}$ , without the intermediate decrease. Figure 3(b) shows impedance behavior as a function of temperature for different frequencies. An increase in resistance with temperature was observed for all the frequencies. Interestingly, the change in resistance was not significant up to 10 kHz. Beyond 10 kHz, the  $Z'$  increased due to the same reasons as that for the as-sintered sample. Figure 3(c) shows  $Z''$  as a function of frequency. The  $Z''$  remained unchanged

as a function of temperature, similar to that for the as-sintered samples showed in Fig. 2(c). The TCR as a function of temperature is shown in Fig. 2(d). The TCR for the post-processed sample was about 0.002  $^{\circ}\text{C}^{-1}$  to 0.0025  $^{\circ}\text{C}^{-1}$  (at 20 Hz) for the range of 24–500  $^{\circ}\text{C}$ , which is closer to the TCR of bulk silver (0.0038  $^{\circ}\text{C}^{-1}$ ). It is yet unclear why the TCR value increased in the post-processed sample. The TCR for the post-processed sample as a function of temperature is shown in Fig. 3(d).

## B. X-ray diffraction

The XRD patterns for the Ag NP films in un-sintered state, sintered at 200  $^{\circ}\text{C}$  for 30 min, sintered at 200  $^{\circ}\text{C}$  for 30 min followed by exposure to 200  $^{\circ}\text{C}$  for 6 h (i.e., post-processed sample), and sintered at 200  $^{\circ}\text{C}$  for 30 min followed by the electrical measurements up to 500  $^{\circ}\text{C}$ , are shown in Fig. 4(a). All peaks correspond to fcc Ag and confirm the crystallinity of the silver NP films. The patterns also confirm that there is no formation of secondary or oxide phases. Figure 4(b) shows the high resolution, detailed scan of the most intense peak for the set of same samples. It can be seen from Fig. 4(a) that the diffraction peak is rather broad for the un-sintered sample indicating a smaller crystallite size. However, it is observed that for the sintered samples the peak width decreased, suggesting the increase in crystallite size due to thermal processing. Such crystallite or grain growth can occur in NP based sintering processes due to aggregative growth<sup>27,28</sup> and Ostwald ripening.<sup>29</sup> The position and shape of the peaks from X-ray diffraction contains valuable information regarding the phase of the materials, size of the crystallite, and the strain in the film. For instance, the

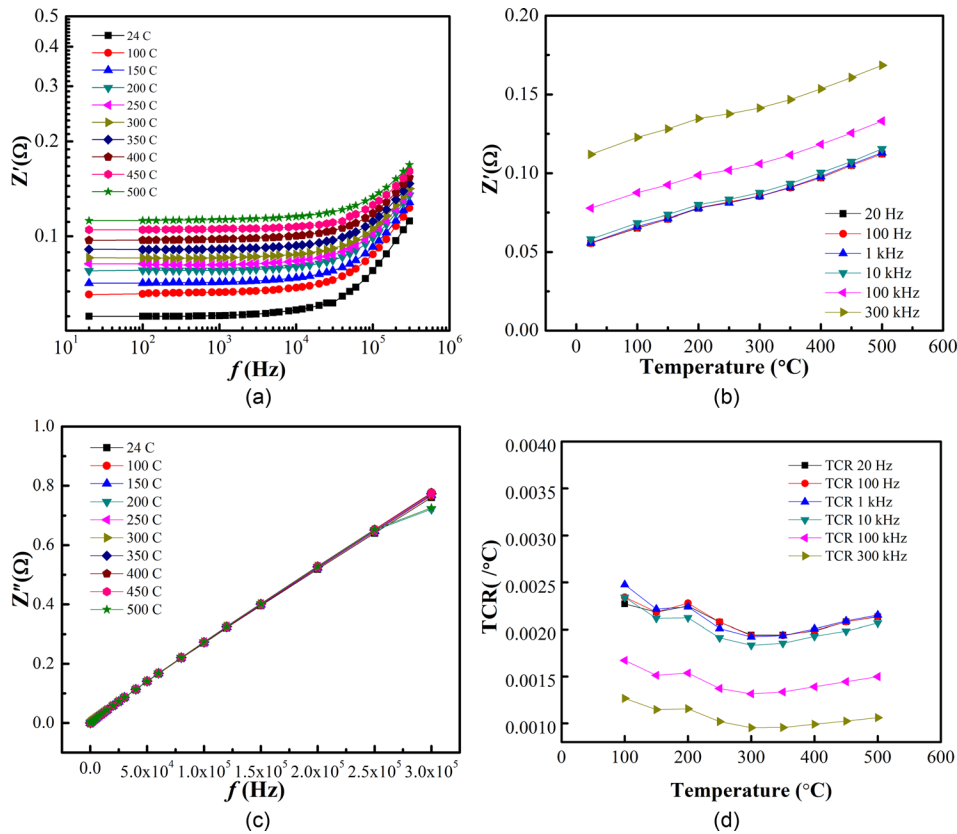


FIG. 3. Electrical behavior of Ag NP film at different temperatures (24 to 500  $^{\circ}\text{C}$ ) and frequencies (0.02–300 kHz). A film sintering condition of 200  $^{\circ}\text{C}$  for 30 min, followed by 200  $^{\circ}\text{C}$  for 6 h was applied prior to the electrical measurements. (a) The real part of impedance ( $Z'$ ) as a function of frequency measured at intervals of about 50  $^{\circ}\text{C}$  for different frequencies. (b) The real part of impedance ( $Z'$ ) as a function of temperature. (c) Imaginary part of impedance ( $Z''$ ) as a function of measurement frequency. (d) TCR as a function of temperature.

shift noted for the (111) peak (Fig. 4(b)) indicates a change in inter-planar spacing and the lattice parameter and hence the strain within the Ag film. The strain and crystallite size of the films was calculated for different conditions using full width at half maximum (FWHM in radians) of the diffraction peaks based on the Williamson-Hall (W-H) plot.<sup>30</sup> However, such peak broadening in an XRD profile is a convolution of lattice strain, distribution of grain size, and instrumental broadening effects. The peak broadening due to the instrument can be removed through calibration with a standard reference material. For the current study, NIST standard  $\text{Cr}_2\text{O}_3$  was used as reference material with crystallite size 380 nm. The following equation was then used for W-H plot<sup>30</sup> in order to calculate microstrain and crystallite size for different conditions:

$$\beta \cos \theta = \frac{0.9\lambda}{D} + 4\epsilon \sin \theta, \quad (2)$$

where micro-strain is  $\epsilon = \frac{\Delta d}{d}$  (%), with  $d$  being the lattice spacing.

Plotting  $\beta \cos \theta$  as function of  $4 \sin \theta$  will yield the slope that gives the strain and the intercept and hence the crystallite size. Figure 4(c) shows the W-H plot for three representative samples. Table I presents the microstrain and crystallite size of the samples determined based on the W-H plots. It can be seen that straight lines were obtained for most of the samples; however, a few discrete data points for the sample sintered for long time and cycled up to 500  $^{\circ}\text{C}$  were observed to be non-linear, which may be due to the irregular grain formation at high temperature. The crystallite size ( $D$ ) of the films was also evaluated based on the Scherer's formula<sup>31</sup>

$$D = \frac{0.9\lambda}{\beta \cos \theta}, \quad (3)$$

where  $D$  is the crystallite size,  $\lambda$  is the X-ray wavelength, and  $\theta$  is the Bragg diffraction angle. The lattice constant,  $a$ , and crystallite size estimated based on the Scherer's formula for different samples are also given in Table I. The crystallite sizes calculated from the W-H plot and Scherer's formula account for the higher and lower limits of the crystallite sizes, respectively. It can be seen that the crystallite size increases and microstrain decreases with longer exposure times. Further, an increase in temperature suffices to decrease residual stress in the film as seen in Table I. It is noted that the grain growth of Ag NPs has been observed when they are sintered for different times at temperatures up to 300  $^{\circ}\text{C}$ .<sup>19</sup> From Fig. 4(a), it can also be seen that the peaks are due to only polycrystalline silver and no extra peaks were detected for silver oxide, indicating that the silver did not oxidize due to the thermal exposure.

### C. X-ray photoelectron spectroscopy

To better understand whether oxidation occurred in the film from high temperature exposure, it was necessary to determine the chemical state of the silver films under different conditions through X-ray photoelectron spectroscopy (XPS). This is particularly important since the sintered nanoparticle films tend to have higher surface-to-volume ratio, and hence higher propensity to oxidation when compared to the films fabricated from bulk of the metals. Additionally, XRD will not detect a second phase of Ag oxide if its volume fraction is very low. Figure 5 shows an XPS plot for Ag

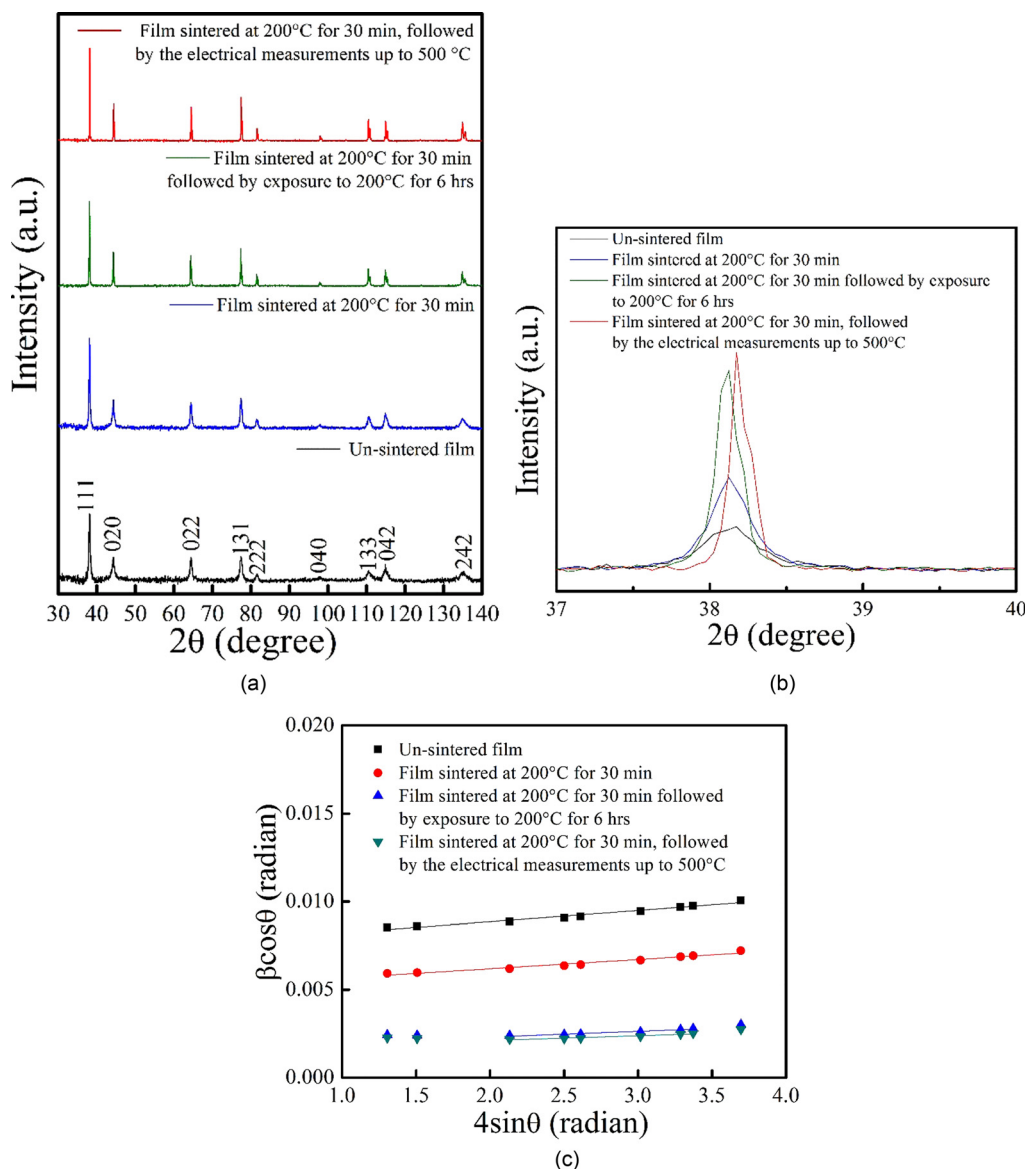


FIG. 4. X-ray Diffraction (XRD) results for Ag NP films that were sintered under different conditions. (a) An XRD scan plot, (b) high-resolution scan of (111) peak, and (c) Williamson-Hull plots.

film under different conditions. The data shown are Ag 3d core-level XPS scans for Ag NP films under various conditions. The scans exhibit a doublet corresponding to Ag 3d spin orbit splitting, i.e., Ag 3d<sub>3/2</sub> and Ag 3d<sub>5/2</sub>. Most notable characteristic feature of these XPS spectra is the presence of Ag 3d peaks without any appreciable change in either peak shape or satellite/secondary peak development. The Ag 3d

doublet matches well with the reported value of binding energy (BE) for metallic Ag.<sup>32</sup> This observation confirms the formation of Ag NP film with chemical purity. Furthermore, no peak shift or change in peak shape due to heating confirms that Ag NP films are stable upon thermal exposure, especially without any oxidation. Note that XPS is very sensitive to the metal-oxygen bond formation as a result of

TABLE I. Lattice constant, unit cell volume, crystallite size, microstrain, and dislocation density for the samples with different thermal histories from the XRD data shown in Fig. 4. (1) Un-sintered sample, (2) sample was sintered at 200°C for 30 min, (3) sample was sintered at 200°C for 30 min followed by exposure to 200°C for 6 hrs, and (4) sample was sintered at 200°C for 30 min followed by electrical measurements up to 500°C. The lattice constant, unit cell volume, and crystallite size (from Scherrer's Eq.) were calculated based on most intense peak (111).

Sample	Lattice constant, $a$ (Å)	Unit cell volume (Å <sup>3</sup> )	Crystallite size, $D$ (W-H) plot (nm)	Crystallite size, $D$ (from Scherrer's Eq.) (nm)	Micro strain (W-H) plot (%)	Dislocation density ( $\delta$ ) (m <sup>-2</sup> )
1	4.08755	68.2952	19.30	16.27	0.000636	$6.15 \times 10^{14}$
2	4.08755	68.2952	28.174	23.38	0.000527	$4.28 \times 10^{14}$
3	4.08835	68.3352	114.028	57.13	0.000455	$1.75 \times 10^{14}$
4	4.07991	67.9130	127.0319	61.18	0.000273	$1.63 \times 10^{14}$

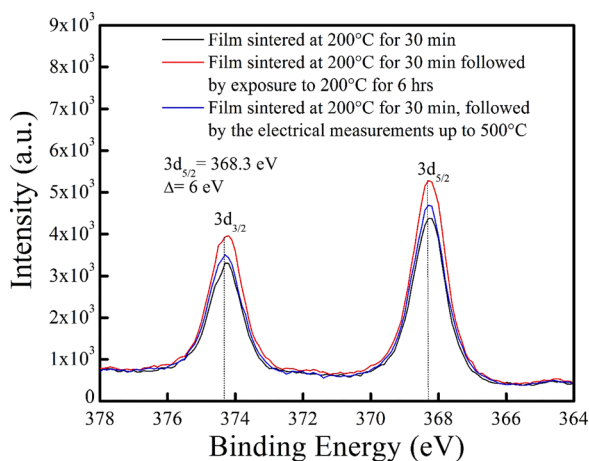


FIG. 5. XPS plot of the printed Ag NP films exposed to different thermal histories. The peaks without any satellite/secondary peak at 3d spin splitting orbital confirms no oxidation of the silver film during the time scale of measurement.

oxidation. Under such conditions, electronic charge redistribution induces peak shift in the metal core-level.<sup>33–35</sup> Thus, the Ag 3d<sub>5/2</sub> peak is expected to experience a BE shift due to oxidation which is not the case for current study indicating that the samples are stable and did not oxidize at high temperature. Generally, the 3d<sub>5/2</sub> peak for Ag (I) in Ag<sub>2</sub>O is found at a BE of 367.7 ± 0.2 eV and for AgO, at a BE of 367.4 ± 0.2 eV.<sup>36</sup> Again, for silver oxides, a broadened full width at half maximum (FWHM) should be observed at the 3d<sub>5/2</sub> peak,<sup>36</sup> which was not the case for the present study. The XPS analysis thus confirms that Ag did not oxidize when exposed to 500 °C or from exposure to ambient air during the time scale of measurements (more than 3 weeks between sintering and XPS measurements).

#### D. Microstructure

The XRD and XPS results already provide clues regarding the impedance behavior observed in Figs. 2 and 3. However, direct microstructural observations of the film after thermal processing can further shed light on the film behavior. Figure 6 shows the representative SEM images at different magnifications of the films sintered at 200 °C for 30 min (Fig. 6(a)), sintered at 200 °C for 30 min then post processed 200 °C for 6 h (Fig. 6(b)), the film in Fig. 6(b), heated up to 500 °C during impedance measurements (Fig. 6(c)), and the film in Fig. 6(a) heated up to 500 °C during impedance measurements (Fig. 6(d)). Figure 6(e) shows a higher magnification image of Fig. 6(c), showing possible directions for the grain boundary migration (indicated by black arrow), surface thermal grooving (indicated by red circle), and void/pin holes (indicated by blue arrows). Figures 6(b)–6(d) indicate an increase in the grain size compared to Fig. 6(a). Figures 6(f) and 6(g) show unmarked and marked higher magnification images of the film surface in Fig. 6(c), where possible twin structures are shown in Fig. 6(g). It should be noted that the particle sizes observed in the SEM top-down images may not be exactly the same as the crystallite size given in Table I as the SEM images are in 2-D and a few crystallites may form a structure that appears as a grain (or vice versa).

The increase in grain size, however, is apparent in Figs. 6(b)–6(d), compared to Fig. 6(a). The grain size in Fig. 6(a) compares well with the starting particle size of 30–50 nm. It is well-known how the sintering mechanism creates bonding in the NP via surface and volume diffusion driven by a chemical potential to form the conductive film.<sup>37–40</sup>

From Fig. 6(e), it was observed that due to thermal exposure, the Ag NP films go through thermal grooving<sup>41</sup> where grain boundaries meet the outer surfaces. The development of such grooves depends upon the surface tension  $\gamma_{Ag/air}$  and the single grain boundary tensions  $\gamma_{gb}$  in such a way that the corresponding surface tensions are resolved along a single line of intersection (shown by the circle in the schematic of Fig. 6(h)) and mathematically related by<sup>41,42</sup>

$$\gamma_{gb} = 2\gamma_{Ag/air} \cos \frac{\theta}{2}. \quad (4)$$

The reported value for such grooving angle was in the range of about 120°–140° for films deposited using evaporation.<sup>42</sup> Figure 6(i) shows an AFM scan of the surface of a sample in Fig. 6(c). The surface topography is seen to capture the grains with the grooving angle in the range of 120°–130°, within the same range of the Ag films deposited using evaporation.<sup>42</sup> This observation indicates that the grain boundary energy is less than the surface energy. It is also noted that the angle is not always the same everywhere, possibly due to the varying Ag-air interface energy with crystal orientation, the adsorbed impurities on the surface (e.g., from escaping binders of the NPs), and the dependence of grain boundary energy on grain misorientation. The importance of such grooves in printed films is that a smaller grooving angle can create a deep groove and rupture a film, especially if the film thickness is < 1 μm. The possibility of film rupture, however, can be mitigated by having multiple printed layers, especially for application in high temperature sensors and antennas. The formation of voids/pinholes mostly at the Ag grain junctions was observed due to thermal grooving (indicated by blue arrow in Fig. 6(e)). According to Presland *et al.*,<sup>43</sup> such surface grooves can also be generated at twin boundaries. Indeed, several possible twin structures were observed as indicated in Fig. 6(g).

It can be noted that the smaller grains of Figs. 6(c) and 6(d) are larger by an order of magnitude than the grains in the as-sintered sample (Fig. 6(a)). Figs. 7(a) and 7(b) show the grain size distribution for the Ag films shown in Figs. 6(a) and 6(c), respectively. In addition to the increase in the grain size, the grain structure in Fig. 6(c) shows a broadened distribution along with a discontinuous or “abnormal” grain growth. The growth of a few grains at the expense of the neighboring grains is a feature commonly observed for bulk silver films<sup>27,42</sup> and is shown to be dependent on the thickness and initial texturing of the film.<sup>27</sup> Indeed, for the AJ printed NP based films in this study, the XRD profile in Fig. 4(a) indicates that the (111) texturing. Furthermore, an increase in the (111) peak intensity (Figs. 4(a) and 4(b)) due to thermal cycling implies that the texturing and grain growth is also dominant along (111) orientation and consistent with the observations on evaporated silver films.<sup>27</sup> One of the possible driving forces for abnormal grain growth is the energy

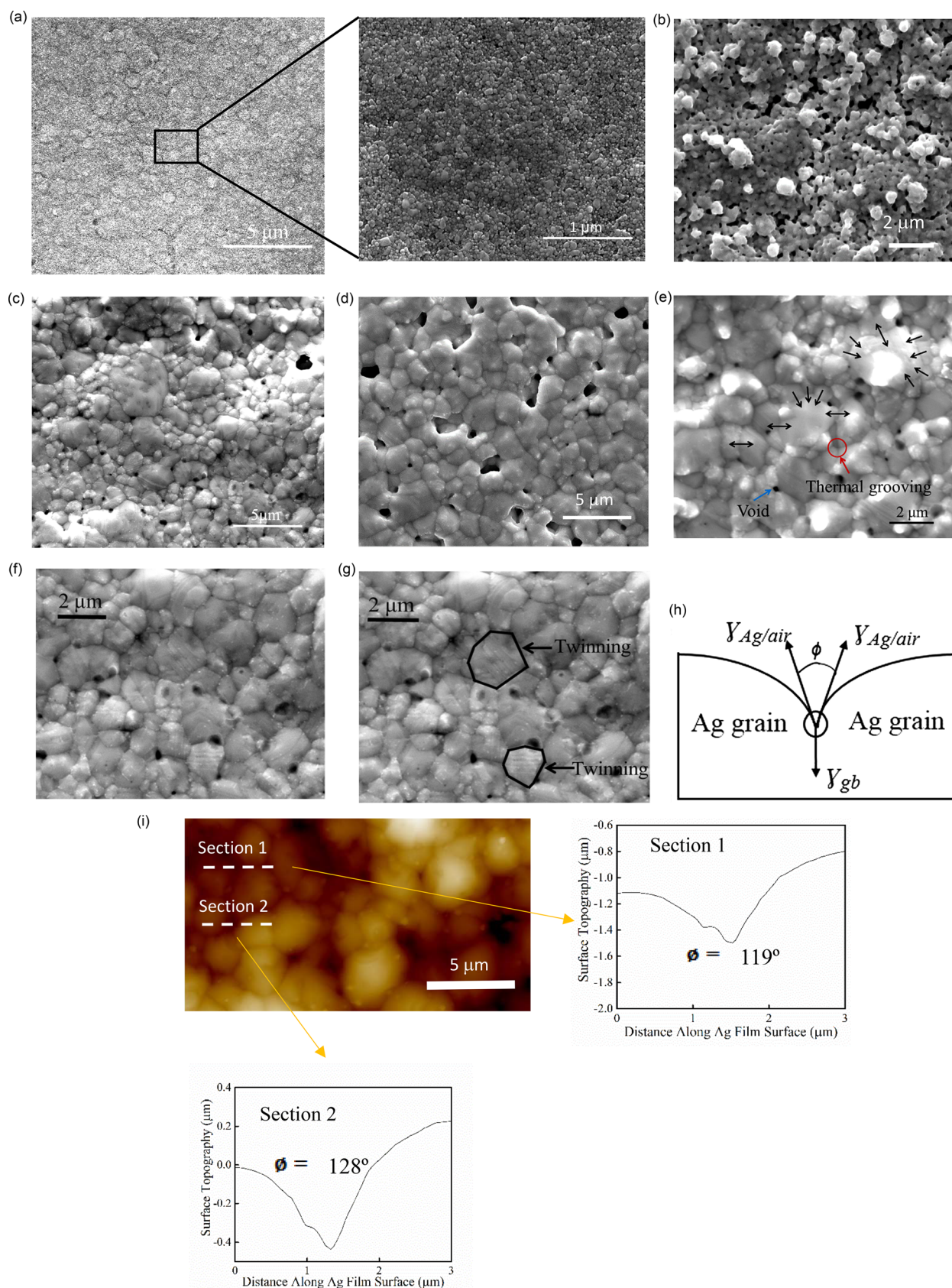


FIG. 6. Representative SEM images of the AJ printed Ag NP films. (a) Top surface morphology of the film sintered at 200 °C for 30 min at different magnifications. (b) Top surface morphology of the film sintered at 200 °C for 30 min, followed by 200 °C for 6 h. (c) Top surface morphology of the film in (b), heated up to 500 °C for impedance measurements. (d) Top surface morphology of the film in (a), heated up to 500 °C for impedance measurements. (e) A higher magnification image of the film surface in (c), showing possible directions for the grain boundary migration (indicated by black arrow), surface thermal grooving (indicated by red circle), and void/pin holes (indicated by blue arrows). (f) A higher magnification image of the film surface in (c). (g) Image showing possible twin in (f). (h) Schematic of the forces causing thermal grooving. (i) AFM scan of the surface of sample (c). The surface topography is seen to capture the grains with the grooving angle,  $\phi$ , in the range of 120–130°.

released from the strain relaxation in the film.<sup>44</sup> Such relaxation is observed in the current study as shown in Table I. For the samples shown in Fig. 6(d), the grain size distribution was more uniform but a few grains did appear to be larger than others. A possible trajectory of the small grains merging into larger grains is indicated by arrows in Fig. 6(e).

### E. Electrical conductivity

Next, we estimate the surface diffusivity from the film microstructural observations using the Brandon and Bradshaw model.<sup>45,46</sup> During grain growth, it is expected that the atoms of the smaller grains on the surface tend to migrate into larger grains by surface diffusion. Due to surface diffusion, the grain growth occurs with thermal grooving and contributes to the formation of pinholes to the system.<sup>45</sup> Based on the grain size, hole size, and time of exposure, the surface diffusion coefficient can be calculated using the following formula:<sup>46</sup>

$$D_s = \frac{2 r^{\frac{5}{2}} h^{\frac{3}{2}} k_B T}{5 \pi^{\frac{1}{2}} t \gamma v \omega^2}, \quad (5)$$

where  $r$  is the hole radius,  $h$  is the film thickness,  $t$  is time of exposure,  $k_B$  is the Boltzmann constant,  $\gamma$  is the surface energy,  $\omega$  is the atomic volume, and  $v$  is the surface density of atoms. We take the values of  $\gamma = 1.2 \times 10^{-4}$  J/cm<sup>2</sup> (for bulk Ag from Nanda<sup>47</sup>),  $\omega = 1.7 \times 10^{-23}$  cm<sup>3</sup> (from the lattice parameter of Ag),<sup>42</sup> and  $v = 1.5 \times 10^{15}$  cm<sup>-2</sup> (Mullins<sup>41</sup>). Taking the hole radii shown in Fig. 6(e), the calculated surface-self diffusion coefficient for Ag is  $1.74 \times 10^{-6}$  cm<sup>2</sup>/s at 500 °C. The estimated value of  $D_s$  for Ag in the current work is one order of magnitude lower than the previously reported value<sup>42</sup> as the  $\gamma$  assumed in this work (from Nanda,<sup>47</sup> which is accurate) is an order of magnitude higher than that assumed in Simrick.<sup>42</sup>

From the above discussion and Table I, it is clear that the films exposed to 500 °C show larger crystallite size (and also grain size) when compared to the as-sintered samples. The sintering conditions of the as-sintered samples are compatible with previous reports<sup>20,25,26</sup> and manufacturer recommendations. As the crystallite size grows, it is expected that the grain boundary (GB) area will reduce significantly. A reduction in the GB area is expected to reduce its contribution to the electron scattering.<sup>48-50</sup> and lower the  $Z'$ . Note, however, that the exact value of resistance increase per unit area of Ag grain boundary is yet unknown. The transition period when the grains grow is thus expected to influence the resistance to current flow as is indeed observed in Figs. 2(a) and 2(b). For the sample post-processed at 200 °C for 6 h, however, the crystallite size is large (Table I) and a stable electrical behavior can be seen in Figs. 3(a) and 3(b). The microstructure, thus, strongly influences the measured high temperature electrical behavior of the Ag NP films with an additional sintering step helping the stabilization of the electrical properties.

Additional defects in the film such as dislocations can also affect the electrical resistivity. Based on FWHM (in radians), the dislocation density ( $\delta$ , in m<sup>-2</sup>) can be estimated using the following equation:<sup>51</sup>

$$\delta = \frac{15\beta \cos \theta}{4aD}. \quad (6)$$

The calculated values of dislocation density are given in Table I. The dislocation density decreased with longer sintering time and an exposure to higher temperature (500 °C). The reason could be the migration of dislocations and/or their partial annihilation due to thermal activation. A reduction in dislocation density is also consistent with the trend seen in the strain relaxation (Table I) as well as the reduced resistance after the sintered sample was taken to 500 °C.

The results presented in the study thus shed light on several important features of the sintered NP films fabricated using the AJ micro-additive method for high temperature applications. First, it is clear that the starting NP size determines the initial microstructure of the film for Ag NP sintering conditions of  $\leq 200$  °C for up to 30 min. The Ag film under these conditions can undergo further grain growth when exposed to high temperature and reduce the scattering of the electrons and thus the  $Z'$  at a temperature range of 150–300 °C. This condition, however, was altered when the initially sintered samples were exposed to 200 °C for 6 h. The resistivity difference between the as-sintered samples (represented by Fig. 6(a)) and that exposed to 500 °C (represented by Fig. 6(d)) can now be used to estimate the grain boundary resistivity using the formula<sup>52,53</sup>

$$\rho = \rho_b + \frac{\rho_{gb} \delta_{gb}}{d}, \quad (7)$$

where  $\rho$  is the measured resistivity,  $\rho_b$  is the bulk resistivity,  $\delta_{gb}$  is the grain boundary width, usually of the order of 1 nm to 10 nm,<sup>52</sup>  $\rho_{gb}$  is the specific grain boundary resistivity, and  $d$  is the size of the grain. Assuming that the bulk resistivity remains constant and taking the grain sizes shown in Fig. 6, the  $\rho_{gb}$  can be estimated to be in a range of  $10^{-7}$  to  $10^{-8}$  Ω-cm for a  $\delta_{gb}$

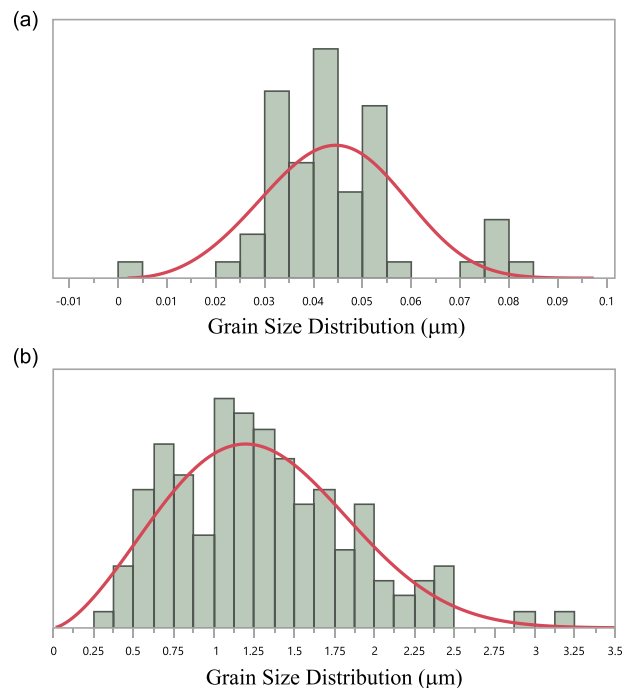


FIG. 7. (a) Grain size distribution for the Ag film shown in Fig. 6(a) with Weibull fit. (b) Grain size distribution for the Ag film shown in Fig. 6(c) with Weibull fit.

of 1 nm and 10 nm, respectively; which is two to three orders of magnitude lower than the Ag bulk resistivity. Note that the  $\rho_{gb}$  values have been reported only at low temperatures (e.g., at 4 K and 77 K)<sup>50,54</sup> and no measurements have been reported under ambient conditions. Finally, we make an attempt to present the mechanism involved based on the results for Ag NP films discussed above. A schematic of the possible mechanism involved in this case is presented in Figs. 8(a)–8(c). Fig. 8(a) shows the Ag NPs in the as-deposited condition, while Figs. 8(b) and 8(c) show the growing film grain size with thermal exposure and its effect on the overall resistivity. Smaller size and more GBs contribute to electrical resistivity in the Ag NP films sintered at lower temperatures. However, when these Ag NP films are sintered at relatively higher temperatures or longer times, the electrical resistivity decreases due to grain size increase coupled with a significant reduction in the GBs.

Thus, from these results and discussion, it is clear that with the increasing usage of printed electronic techniques, the electrical stability of the fabricated films will be highly important and the grain size effect will have to be taken into account in designing the electrical circuits. Most notable feature is that by carefully controlling the thermal conditions, AJ printed Ag NP films with enhanced thermal stability and oxidation resistance up to 500 °C appear to be promising for

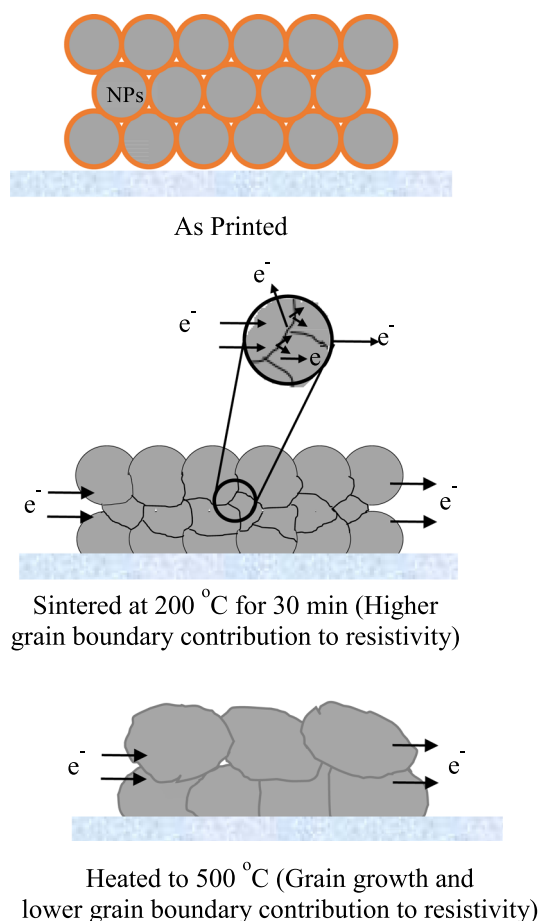


FIG. 8. Schematic showing (a) the as deposited Ag NP film using Aerosol Jet technique. (b) Sintering and grain size close to the initial NP dimensions. (c) Grain growth when exposed to 500 °C, resulting in a reduction in the contribution of the grain boundary resistance to the total resistance.

the desired high temperature sensor applications, which usually span in the range of 300–500 °C for such metal electrodes.

#### IV. SUMMARY AND CONCLUSIONS

An approach is presented to successfully synthesize silver NP films with controlled structure and properties using Aerosol Jet printing method, which is an emerging platform under additive manufacturing of materials for next generation technological applications. The microstructure, electrical properties, high-temperature stability, and oxidation resistance of AJ printed Ag metal NP films were studied in detail under the variable sintering conditions. The electrical behavior evaluated using impedance spectroscopic measurements indicate that the microstructure strongly influences the electrical characteristics of the Ag NP films. XRD, XPS, and electrical measurements demonstrate that a careful choice of sintering conditions could provide efficient means to control the temperature stability and oxidation resistance of the Ag NP films up to a temperature of 500 °C, which is more than sufficient for the desired set of energy or electronics applications.

#### ACKNOWLEDGMENTS

This work was supported by the U.S. Department of Energy, National Energy Technology Laboratory (NETL), under Grant No. DE-FE0026170. We would like to thank Mr. Jose Marcial at WSU for XRD measurements.

- <sup>1</sup>S. Chu and A. Majumdar, *Nature* **488**, 294 (2012).
- <sup>2</sup>W. C. Wilson and G. M. Atkinson, *IEEE Sens. J.* **14**, 3745 (2014).
- <sup>3</sup>R. R. Romanosky and S. M. Maley, in *Harsh Environment Sensor Development for Advanced Energy Systems* (SPIE, 2013), p. 87250H.
- <sup>4</sup>J. Watson and G. Castro, *J. Mater. Sci.: Mater. Electron.* **26**, 9226 (2015).
- <sup>5</sup>D. Espalin, D. W. Muse, E. MacDonald, and R. B. Wicker, *Int. J. Adv. Manuf. Technol.* **72**, 963 (2014).
- <sup>6</sup>A. Kamyshny and S. Magdassi, *Small* **10**, 3515 (2014).
- <sup>7</sup>E. MacDonald, R. Salas, D. Espalin, M. Perez, E. Aguilera, D. Muse, and R. B. Wicker, *IEEE Access* **2**, 234 (2014).
- <sup>8</sup>J. M. Hoey, A. Lutfurakhmanov, D. L. Schulz, and I. S. Akhatov, *J. Nanotechnol.* **2012**, 1–22 (2012).
- <sup>9</sup>M. T. Rahman, L. Renaud, M. Renn, D. Heo, and R. Panat, *J. Micromech. Microeng.* **25**, 107002 (2015).
- <sup>10</sup>H. Yang, M. T. Rahman, D. Du, R. Panat, and Y. Lin, *Sens. Actuators, B* **230**, 600 (2016).
- <sup>11</sup>S. Li, J. G. Park, S. Wang, R. Liang, C. Zhang, and B. Wang, *Carbon* **73**, 303 (2014).
- <sup>12</sup>C. S. Jones, X. Lu, M. Renn, M. Stroder, and W.-S. Shih, *Microelectron. Eng.* **87**, 434 (2010).
- <sup>13</sup>A. Mette, P. Richter, M. Hörteis, and S. Glunz, *Prog. Photovoltaics: Res. Appl.* **15**, 621 (2007).
- <sup>14</sup>C. Yang, E. Zhou, S. Miyayoshi, K. Hashimoto, and K. Tajima, *ACS Appl. Mater. Interfaces* **3**, 4053 (2011).
- <sup>15</sup>C. Goth, S. Putzo, and J. Franke, *Aerosol Jet Printing on Rapid Prototyping Materials for Fine Pitch Electronic Applications* (IEEE, 2011), p. 1211.
- <sup>16</sup>T. L. Alford, D. Adams, T. Laursen, and B. Manfred Ullrich, *Appl. Phys. Lett.* **68**, 3251 (1996).
- <sup>17</sup>H. C. Kim, T. L. Alford, and D. R. Allee, *Appl. Phys. Lett.* **81**, 4287 (2002).
- <sup>18</sup>S. K. Sharma and J. Spitz, *Thin Solid Films* **65**, 339 (1980).
- <sup>19</sup>T. Seifert, E. Sowade, F. Roscher, M. Wiemer, T. Gessner, and R. R. Baumann, *Ind. Eng. Chem. Res.* **54**, 769 (2015).
- <sup>20</sup>S. K. Volkman, S. Yin, T. Bakhishev, K. Puntambekar, V. Subramanian, and M. F. Toney, *Chem. Mater.* **23**, 4634 (2011).

- <sup>21</sup>J. R. Greer and R. A. Street, *Acta Mater.* **55**, 6345 (2007).
- <sup>22</sup>M. J. Renn, M. Essien, B. H. King, and J. A. Paulsen, in *USPTO*, Optomec Design Company, US, #7674671 B2 (2010); available at <https://www.google.com/patents/US7674671>.
- <sup>23</sup>X. Qin, W. Zhang, L. Zhang, L. Jiang, X. Liu, and D. Jin, *Phys. Rev. B* **56**, 10596 (1997).
- <sup>24</sup>C. Kittel, *Introduction to Solid State Physics* (Wiley, 2004).
- <sup>25</sup>M. T. Rahman, A. Rahimi, S. Gupta, and R. Panat, *Sens. and Actuat. A: Physical* **248**, 94–103 (2016).
- <sup>26</sup>W. Shen, X. Zhang, Q. Huang, Q. Xu, and W. Song, *Nanoscale* **6**, 1622 (2014).
- <sup>27</sup>J. Greiser, P. Müllner, and E. Arzt, *Acta Mater.* **49**, 1041 (2001).
- <sup>28</sup>R. L. Penn and J. F. Banfield, *Science* **281**, 969 (1998).
- <sup>29</sup>F. Huang, H. Zhang, and J. F. Banfield, *Nano Lett.* **3**, 373 (2003).
- <sup>30</sup>Z. Shao, S. Saitzek, A. Ferri, M. Rguiti, L. Dupont, P. Roussel, and R. Desfeux, *J. Mater. Chem.* **22**, 9806 (2012).
- <sup>31</sup>A. R. Bushroa, R. G. Rahbari, H. H. Masjuki, and M. R. Muhamad, *Vacuum* **86**, 1107 (2012).
- <sup>32</sup>D. Briggs, *Surf. Interface Anal.* **3**, 190 (1981).
- <sup>33</sup>C. V. Ramana, E. J. Rubio, C. D. Barraza, A. Miranda Gallardo, S. McPeak, S. Kotru, and J. T. Grant, *J. Appl. Phys.* **115**, 043508 (2014).
- <sup>34</sup>C. V. Ramana, V. V. Atuchin, V. Kesler, V. Kochubey, L. Pokrovsky, V. Shutthanandan, U. Becker, and R. C. Ewing, *Appl. Surf. Sci.* **253**, 5368 (2007).
- <sup>35</sup>B. Aguirre, R. Vemuri, D. Zubia, M. H. Engelhard, V. Shutthanandan, K. K. Bharathi, and C. V. Ramana, *Appl. Surf. Sci.* **257**, 2197 (2011).
- <sup>36</sup>T. C. Kaspar, T. Droubay, S. A. Chambers, and P. S. Bagus, *J. Phys. Chem. C* **114**, 21562 (2010).
- <sup>37</sup>K. Sieradzki, K. Bailey, and T. L. Alford, *Appl. Phys. Lett.* **79**, 3401 (2001).
- <sup>38</sup>A. Hu, J. Y. Guo, H. Alarifi, G. Patane, Y. Zhou, G. Compagnini, and C. X. Xu, *Appl. Phys. Lett.* **97**, 153117 (2010).
- <sup>39</sup>P. Peng, A. Hu, A. P. Gerlich, G. Zou, L. Liu, and Y. N. Zhou, *ACS Appl. Mater. Interfaces* **7**, 12597 (2015).
- <sup>40</sup>C. Yang, C. P. Wong, and M. M. F. Yuen, *J. Mater. Chem. C* **1**, 4052 (2013).
- <sup>41</sup>W. W. Mullins, *J. Appl. Phys.* **28**, 333 (1957).
- <sup>42</sup>N. J. Simrick, J. A. Kilner, and A. Atkinson, *Thin Solid Films* **520**, 2855 (2012).
- <sup>43</sup>A. E. B. Presland, G. L. Price, and D. L. Trimm, *Prog. Surf. Sci.* **3**(1), 63 (1972).
- <sup>44</sup>E. J. Mittemeijer, *Fundamentals of Materials Science* (Springer, 2010).
- <sup>45</sup>F. Bradshaw, R. Brandon, and C. Wheeler, *Acta Metall.* **12**, 1057 (1964).
- <sup>46</sup>R. Brandon and F. Bradshaw, Royal Aircraft Establishment Research Report No. 66095 (1966).
- <sup>47</sup>K. K. Nanda, A. Maisels, F. E. Kruis, H. Fissan, and S. Stappert, *Phys. Rev. Lett.* **91**, 106102 (2003).
- <sup>48</sup>R. Dannenberg and A. H. King, *J. Appl. Phys.* **88**, 2623 (2000).
- <sup>49</sup>A. F. Mayadas and M. Shatzkes, *Phys. Rev. B* **1**, 1382 (1970).
- <sup>50</sup>P. Andrews, M. West, and C. Robeson, *Philos. Mag.* **19**, 887 (1969).
- <sup>51</sup>Y. P. V. Subbaiah, P. Prathap, and K. T. R. Reddy, *Appl. Surf. Sci.* **253**, 2409 (2006).
- <sup>52</sup>J. Wang, A. Du, D. Yang, R. Raj, and H. Conrad, *J. Ceram.* **2013**, Article ID 370603, 1 (2013).
- <sup>53</sup>P. Shewmon, *Diffusion in Solids*, 2nd ed. (Metals & Materials Society, 1989).
- <sup>54</sup>M. Kasen, *Philos. Mag.* **21**, 599 (1970).